

# UC Santa Cruz

## UC Santa Cruz Previously Published Works

### Title

Carbon decorated  $\text{Li}_3\text{V}_2(\text{PO}_4)_3$  for high-rate lithium-ion batteries: Electrochemical performance and charge compensation mechanism

### Permalink

<https://escholarship.org/uc/item/0c78t981>

### Authors

Ding, Manling  
Cheng, Chen  
Wei, Qiulong  
[et al.](#)

### Publication Date

2021-02-01

### DOI

10.1016/j.jchem.2020.04.020

Peer reviewed

# **Carbon decorated $\text{Li}_3\text{V}_2(\text{PO}_4)_3$ for high-rate lithium-ion batteries: Electrochemical performance and charge compensation mechanism**

Manling Ding<sup>a</sup>, Chen Cheng<sup>a</sup>, Qiulong Wei<sup>b,\*</sup>, Yue Hu<sup>a</sup>, Yingying Yan<sup>a</sup>, Kehua Dai<sup>c</sup>, Jing Mao<sup>d</sup>,  
Jinghua Guo<sup>e,f</sup>, Liang Zhang<sup>a,\*</sup>, Liqiang Mai<sup>g,\*</sup>

<sup>a</sup>*Institute of Functional Nano & Soft Materials (FUNSOM), Jiangsu Key Laboratory for Carbon-Based Functional Materials & Devices, Soochow University, Suzhou 215123, Jiangsu, China*

<sup>b</sup>*Department of Materials Science and Engineering, Fujian Key Laboratory of Materials Genome, College of Materials, Xiamen University, Xiamen 361005, Fujian, China*

<sup>c</sup>*College of Chemistry, Tianjin Normal University, Tianjin 300387, China*

<sup>d</sup>*School of Materials Science and Engineering, Zhengzhou University, Zhengzhou 450001, Henan, China*

<sup>e</sup>*Advanced Light Source, Lawrence Berkeley National Laboratory, Berkeley, California 94720, USA*

<sup>f</sup>*Department of Chemistry and Biochemistry, University of California, Santa Cruz, California 95064, USA*

<sup>g</sup>*State Key Laboratory of Advanced Technology for Materials Synthesis and Processing, International School of Materials Science and Engineering, Wuhan University of Technology, Wuhan 430070, Hubei, China*

\*Corresponding authors. Email addresses: [liangzhang2019@suda.edu.cn](mailto:liangzhang2019@suda.edu.cn) (L. Zhang); [mlq518@whut.edu.cn](mailto:mlq518@whut.edu.cn) (L. Mai); [qlwei@xmu.edu.cn](mailto:qlwei@xmu.edu.cn) (Q. Wei).

## Abstract

Fast charging and high-power delivering batteries are highly demanded in mobile electronics, electric vehicles and grid energy storage, but there are full of challenges. The star-material  $\text{Li}_3\text{V}_2(\text{PO}_4)_3$  is demonstrated as a promising high-rate cathode material meeting the above requirements. Herein, we report the carbon decorated  $\text{Li}_3\text{V}_2(\text{PO}_4)_3$  (LVP/C) cathode prepared via a facile method, which displays a remarkable high-rate capability and long-term cycling performance. Briefly, the prepared LVP/C delivers a high discharge capacity of  $122 \text{ mAh g}^{-1}$  (~93% of the theoretical capacity) at a high rate up to 20 C and a superior capacity retention of 87.1% after 1000 cycles. Importantly, by applying a combination of X-ray absorption spectroscopy and full-range mapping of resonant inelastic X-ray scattering, we clearly elucidate the structural and chemical evolutions of LVP upon various potentials and cycle numbers. We show unambiguous spectroscopic evidences that the evolution of the hybridization strength between V and O in LVP/C as a consequence of lithiation/delithiation is highly reversible both in the bulk and on the surface during the discharge-charge processes even over extended cycles, which should be responsible for the remarkable electrochemical performance of LVP/C. Our present study provides not only an effective synthesis strategy but also deeper insights into the surface and bulk electrochemical reaction mechanism of LVP, which should be beneficial for the further design of high-performance LVP electrode materials.

**Keywords:** Lithium-ion batteries;  $\text{Li}_3\text{V}_2(\text{PO}_4)_3$ ; Charge compensation mechanism; X-ray absorption spectroscopy; Resonant inelastic X-ray scattering

## 1. Introduction

Rechargeable lithium-ion batteries (LIBs) play important roles in various applications, such as mobile electronics, (hybrid) electric vehicles, and large-scale grid energy storage [1–3]. However, electrode materials with superior electrochemical performance, including safety, energy density, cost and rate performance, are highly desired for better user experiences [4,5]. Transition-metal phosphates (TMPs) are proposed as highly prospective cathodes for LIBs mainly due to their high theoretical energy density, low price, and excellent safety performance [6–11]. Amongst different TMPs, monoclinic  $\text{Li}_3\text{V}_2(\text{PO}_4)_3$  (LVP) supplies a 3D pathway for  $\text{Li}^+$  diffusion because of its lithium super ionic conductor structure, yielding a high ion diffusion coefficient ( $10^{-9}\sim 10^{-10} \text{ cm}^2 \text{ s}^{-1}$ ) [12,13]. However, LVP exhibits a poor electron conductivity ( $2.4\times 10^{-7} \text{ S cm}^{-1}$ ) induced by the separated  $\text{VO}_6$  octahedral arrangement, which significantly limits its commercialization process [13–15]. Previously, different strategies have been proposed to improve the electrochemical performance of LVP (e.g. surface coating [16], element doping [17], decrease of particle size [15,18,19], optimization of synthesized methods [20–22]). However, the corresponding charge compensation mechanism of LVP, especially for the faradaic reactions at the surface and in the bulk during the discharge/charge process, is still poorly understood, which is indispensable for the further improvement of the cyclability and rate capability for LIBs.

Soft X-ray absorption spectroscopy (sXAS) and resonant inelastic X-ray scattering (RIXS) are element specific techniques that can be used to investigate the electronic and structural changes in the battery electrode materials [23,24]. Depending on the detection method, sXAS can be either surface sensitive (total-electron-yield method (TEY) with a detection depth of  $\sim 5 \text{ nm}$ ) or bulk sensitive (total-fluorescence-yield (TFY) with a detection depth of  $\sim 100 \text{ nm}$ ), which enables

XAS as a probe of distinguishing the surface and bulk reactions in battery electrode materials [25,26]. Using sXAS with both TEY and TFY modes, it has been revealed that part of the charge compensation of high-capacity  $\text{Na}_{0.78}\text{Ni}_{0.23}\text{Mn}_{0.69}\text{O}_2$  electrode during the first cycle takes place at the lattice oxygen site, resulting in a bulk to surface transition metal gradient, as evidenced by the gradual decrease of the  $L_{3\text{high}}$  to  $L_{3\text{low}}$  ratio when going from TFY to TEY mode in Ni L-edge sXAS spectra [27]. In contrast, RIXS is a complementary technique to XAS, which could decipher the different component buried in the sXAS spectra [28,29]. In our previous reports, we have clearly revealed the charge compensation mechanism of different electrode materials by using a combination sXAS and RIXS [26,30].

In this work, we aim to tackle both the electrochemical performance and reaction mechanism of LVP for LIBs. The as-prepared carbon decorated  $\text{Li}_3\text{V}_2(\text{PO}_4)_3$  (LVP/C) using a facile method demonstrates an outstanding rate capability and long-term cycling performance with a capacity of  $106 \text{ mAh g}^{-1}$  after 1000 cycles at a high rate to 20 C. By using a combination of surface- and bulk-sensitive XAS and full-range mapping of resonant inelastic X-ray scattering (mRIXS), we clearly reveal the high reversibility of the hybridization strength between V and O in LVP/C occurred both at the surface and bulk during the lithiation/delithiation process even over extended cycles, which should be responsible for the outstanding electrochemical performance of LVP. Our results broaden the fundamental understanding of the charge compensation mechanism of LVP, which is significantly important for the further optimization of LVP materials and the search for new high-performance electrode materials for LIBs.

## **2. Experimental**

### *2.1. Synthesis of LVP/C*

Vanadium pentoxide (2 mmol) and oxalic acid (6 mmol) were dissolved in water (10 mL) at 80 °C under stirring until the solution turned into blue color. Then glucose (2 mmol), lithium acetate (6 mmol) and ammonium dihydrogen phosphate (6 mmol) were slowly added into the blue solution step by step. Ethylene glycol (20 mL) was dropped into above solution and kept stirring for another 1 h. The mixed solution was totally dried, and the obtained powders were fully grounded. Finally, the dried powders were annealed to 750 °C for 6 h under Ar atmosphere with a heating rate of 5 °C min<sup>-1</sup> to yield carbon decorated LVP.

## *2.2. Characterizations and electrochemical measurements*

XRD patterns were collected by using a D8 Advance X-ray diffractometer with Cu K $\alpha$  X-Ray source. FESEM images were collected by using a JEOL JSM-7100F. The carbon content was determined by the CHN element analysis (Elemental Analyzer Company, model: Vario EL cube). For LVP/C electrode, a slurry was obtained by mixing 80 wt% active material, 10 wt% conductive carbon (Super P) and 10 wt% polyvinylidene fluoride (PVDF) binder. N-methyl-2-pyrrolidone (NMP) was used as the medium and the slurry was coated on Al foils. The electrode slurry was dried in a vacuum oven at 120 °C. The mass loading of active material in electrode is ~2.0 mg cm<sup>-2</sup>. The electrochemical measurements were carried out by assembly of 2032 coin cells in a glove box filled with pure argon gas with lithium foil as the counter/reference electrode and 1 M solution of LiPF<sub>6</sub> in ethylene carbonate (EC)/dimethyl carbonate (DMC) as the electrolyte. The specific capacity was calculated based on the total weight of LVP and the carbon coating composites. Galvanostatic rate performance and cyclic voltammetry (CV) were performed by using Bio-Logic potentiostat (VMP3). Long-term cycles were measured by using a battery testing system (NEWARE CT-4008).

### 2.3. Ex-situ XAS and RIXS measurements

The XAS measurements were performed at beamline 8.0.1 of the Advanced Light Source, beamline 02B02 of the Shanghai Synchrotron Radiation Facility, and beamline 16A of Taiwan Light Source. The electrodes at different states of charge were disassembled and rinsed with propylene carbonate thoroughly to remove the surface residue. A home-made suitcase was used to directly transfer the samples from glovebox to beamline without the exposure to air to avoid the change of oxidation states of cycled electrodes [31]. The XAS spectra were normalized first by the incoming beam intensity and then to the absorption pre- and post-edges. The mRIXS data were collected through the ultra-high-efficiency modular spectrometer at beamline 8.0.1 with an excitation energy step of 0.2 eV. The final 2D images were achieved through a data process involving normalization to the beam flux and collection time, integration, and combination.

## 3. Results and discussion

### 3.1 Structure characterizations

The X-ray diffraction (XRD) pattern of the LVP/C sample (Fig. 1a) is fully indexed to the monoclinic LVP phase (JCPDS No. 01-072-7074; space group:  $P2_1/n$ ,  $a = 8.606 \text{ \AA}$ ,  $b = 8.592 \text{ \AA}$ ,  $c = 12.037 \text{ \AA}$ , and  $\beta = 90.61^\circ$ ), suggesting a high purity and crystalline structure of as-synthesized samples [32,33].

Fig. 1(b) schematically depicts the crystal structure of monoclinic LVP interconnected by the “lantern” units  $[V_2(PO_4)_3]$ . Note that, the  $VO_6$  octahedra interlinks with the  $PO_4$  tetrahedra via oxygen atoms, which builds the three-dimensional (3D) network, while lithium atoms flow in the interstitial voids [33,34]. The 3D pathway has been proven to afford a very high ion diffusion coefficient (from  $10^{-9}$  to  $10^{-10} \text{ cm}^2 \text{ s}^{-1}$ ) for fast  $Li^+$  insertion/extraction [35]. The morphology of

LVP/C sample is achieved by field-emission scanning electron microscopy (SEM). As shown in Fig. 1(c and d), the LVP/C particles are integrated together and embedded in a carbon matrix. The carbon content is  $\sim 5.8\%$  according a CHN element analysis [12]. The carbon layers covered on the LVP grains could overcome the intrinsic poor electronic conductive of the phosphate compounds, providing continuous electron transport path for high rate operation.

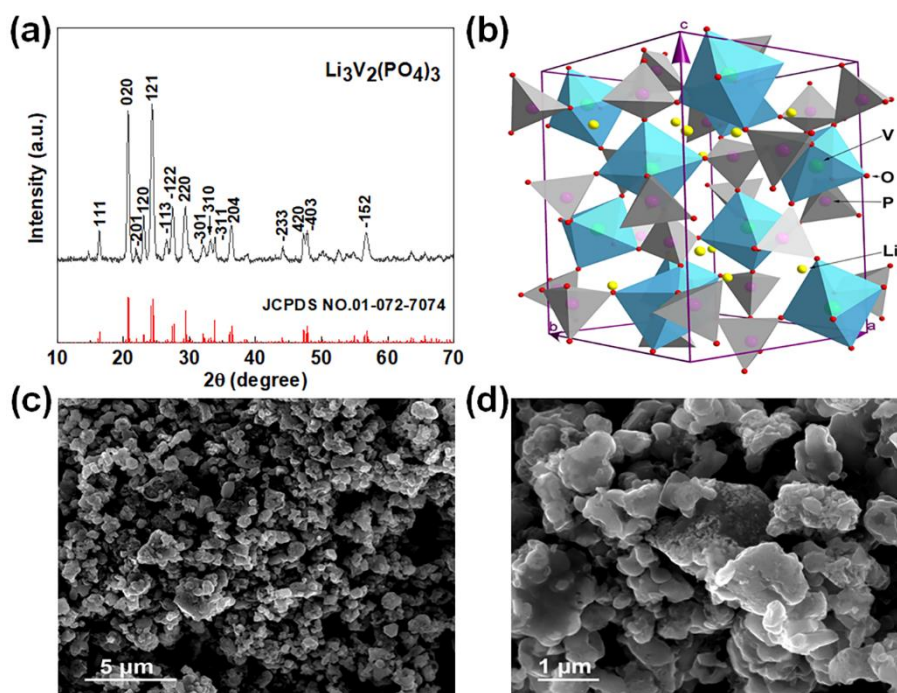
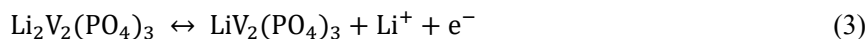
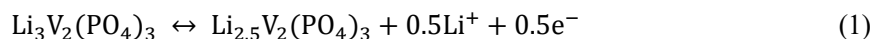


**Fig. 1.** Structure of the as-prepared LVP/C material. (a) XRD patterns, (b) crystal structure, (c, d) SEM images with different magnifications.

### 3.2 Electrochemical measurements

The electrochemical performance of as-prepared materials was investigated by assembling coin cells (2032-type) with the LVP/C as the working electrode and lithium foil as the counter and reference electrode. Galvanostatic charge and discharge in a potential range of 3.0–4.3 V at a rate of 1 C were tested firstly. The charge-discharge profiles of LVP/C (Fig. 2a) show three pairs of plateaus located at 3.596/3.571, 3.679/3.652 and 4.050/4.082 V, which are related to the following three reversible phase transitions during lithium intercalation and extraction (Eqs. 1–3),

respectively [33,36,37].



In addition, the cyclic voltammetry curve of LVP/C at a scan rate of  $0.1 \text{ mV s}^{-1}$  (Fig. 2b) displays three pairs of anodic and cathodic peaks, which are consistent with the charge-discharge profiles.

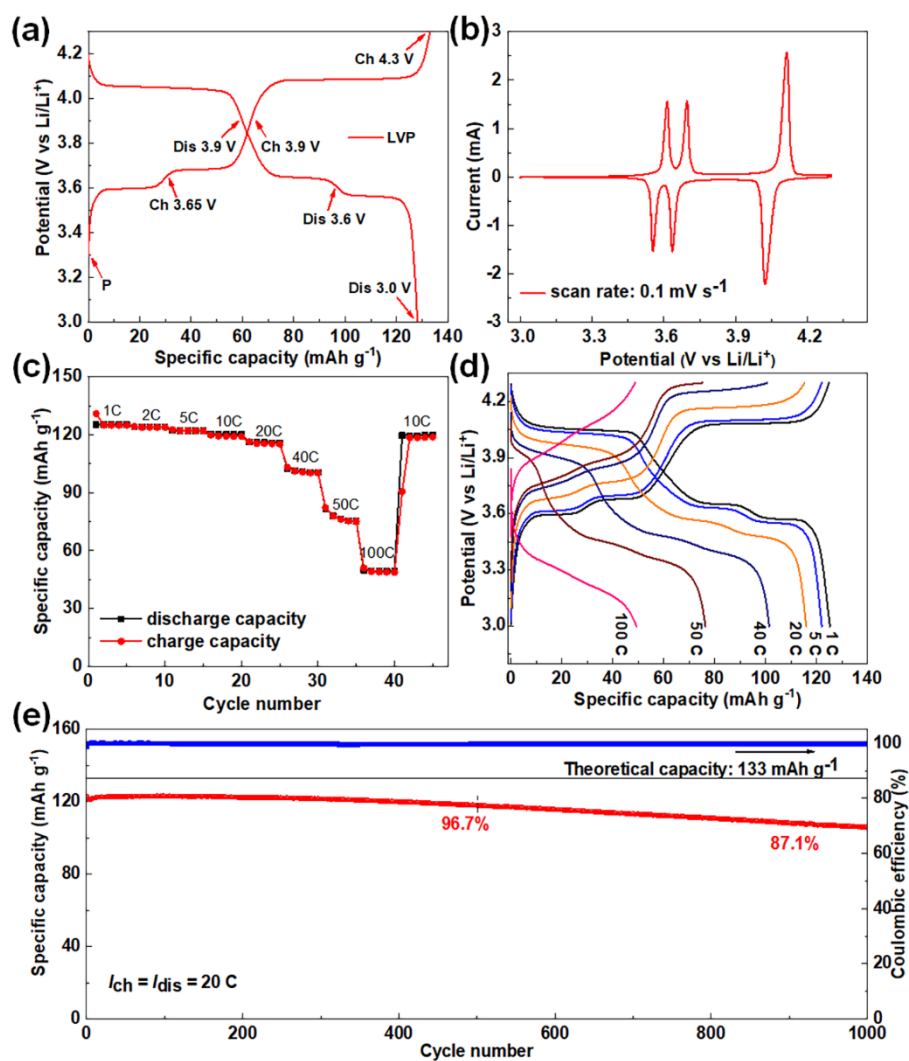


**Fig. 2.** Electrochemical performance of LVP/C. (a) The initial charge-discharge profiles at 1 C in the potential range of 3.0 to 4.3 V vs. Li/Li<sup>+</sup>. The arrows mark the different states of charge tested by XAS and mRIXS. (b) Cyclic voltammetry curve at a scan rate of  $0.1 \text{ mV s}^{-1}$ . (c) Rate

performance. (d) Charge-discharge profiles at various C rates. (e) Long-term cycling performance at 20 C.

The rate performance of the LVP/C cathode is presented in Fig. 2(c and d). At the rates below 20 C, the LVP/C delivers a very close capacity higher than 120 mAh g<sup>-1</sup>. With increasing the rate to 40, 50 and 100 C, corresponding to a charge/discharge time of ~68, 42 and 14 s, the electrode can still deliver a high capacity of 101, 78 and 50 mAh g<sup>-1</sup>, respectively. In addition, 99.0% of the initial capacity is recovered when the rate changes back to 10 C, which strongly indicates the excellent rate capability of LVP/C electrode. It should be noted that with the increase of charge/discharge rate, the overpotential gap between plateaus voltage gradually becomes more serious with the decrease of plateaus length. However, the related charge-discharge plateaus are still apparent under the current density of 50 C, implying the low polarization and excellent ionic diffusion rate of LVP/C [38]. The LVP/C also demonstrates a superior long-term cycling stability with a remarkable capacity of 118 and 106 mAh g<sup>-1</sup> after 500 and 1000 cycles at a high rate of 20 C (Fig. 2e), corresponding to a capacity retention of 96.7% and 87.1%, respectively. The high capacity retention is likely associated with the unique structure of LVP/C, which can not only provide fast electron transport and 3D ionic diffusion pathway but also accommodate the volume change and prevent the dissolution of vanadium during cycling [33,39–41]. Overall, the LVP/C sample exhibits an outstanding rate performance and long-life cycling capability, which makes it a promising candidate for high-performance LIBs. To further unambiguously reveal the charge compensation mechanism of LVP, synchrotron-based X-ray experiments (i.e., XAS and mRIXS) were conducted for LVP/C electrodes at different states of charge (SOCs) and cycle numbers [23,42]. Note that for ex-situ sXAS and mRIXS analyses, all the samples were

electrochemically cycled to various SOCs and then disassembled and rinsed with propylene carbonate to lock the SOCs and remove any surface residue prior to measurement.

### *3.3 Charge compensation mechanism*

Synchrotron-based XAS is an element specific technique, which can detect species that are either crystalline or amorphous. Depending on the detection method, XAS can be either surface sensitive or bulk sensitive, which enables XAS as a probe of distinguishing the surface and bulk reactions in battery electrode materials [43]. We first measured V L-edge and O K-edge XAS of LVP/C (Fig. 3) collected at different SOCs as marked in Fig. 2(a) by recording both TEY and TFY spectra, which can directly probe the evolution of unoccupied V  $3d$  and O  $2p$  states, respectively [23,24,31]. It should be noted that the different overall spectral shape between TEY and TFY results may be related to the presence of self-absorption effect in TFY because it is a photon-in-photon-out detection mode. For V L-edge XAS (Fig. 3(b and c)), the two main features located at 513–521 eV and 521–28 eV are attributed to the V  $2p_{3/2} \rightarrow V 3d$  transition (V  $L_3$ ) and the V  $2p_{1/2} \rightarrow V 3d$  transition (V  $L_2$ ), respectively. The splitting of these two features is related to the core-hole spin orbital coupling effect [28,44]. In addition, the presence of the fine pre-edge structures of  $L_3$ -edge (marked with dash lines in Fig. 3(a and b); the enlarged pre-edge structures are shown in Fig. S3), which are related to the coordination environment of V atoms, implies the deviations from crystallographically equivalent V sites and the formation of the distorted  $VO_6$  octahedra as a result of the strong orbital mixing between V  $3d$  and O  $2p$  states [45,46]. Because of the shorter lifetime and the Coster-Kronig decay process, the line shape of  $L_2$ -edge is broader than that of  $L_3$ -edge, and therefore, we will mainly focus on the spectral shape change of  $L_3$ -edge

for both TEY and TFY spectra (Fig. 3(b and c)).

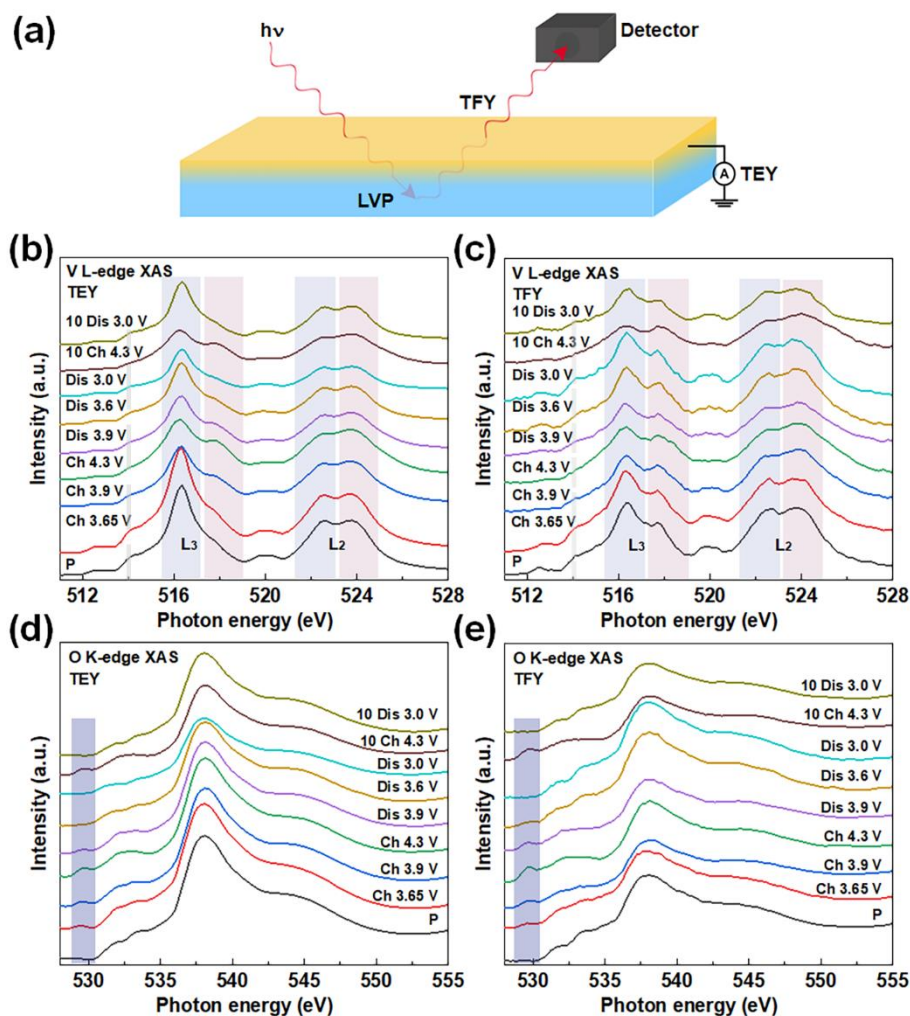


**Fig. 3.** Ex-situ XAS characterization of LVP/C at different SOCs. (a) Schematic illustration of XAS with surface-sensitive TEY and bulk-sensitive TFY. (b, c) V L-edge XAS in TEY and TFY modes. The gray dashed lines mark the pre-edge features. (d, e) O K-edge XAS in TEY and TFY modes.

The V  $L_3$ -edge XAS spectral shape changes gradually as a function of SOC. Specifically, during the first charge process, the weight of the  $L_3$ -edge is gradually redistributed with the increase of the high energy feature, which can be interpreted by the unoccupied  $d$ -character as a function of SOC. The delithiation process results in an increased unoccupancy of V  $3d$  band and

thus the average oxidation state [47,48]. In addition, the disappearance of the pre-edge feature during the charge process suggests that not only the oxidation state but also the atomic arrangement is varied [49]. In the subsequent discharge process back to 3.0 V, the line shape of the V L<sub>3</sub>-edge XAS is fully recovered to that of pristine LVP, indicating the highly reversible redox reaction of V and the stable crystal framework during the charge/discharge process [40,50]. The highly reversible oxidation/reduction of V during the charge/discharge process was also obtained after ten cycles (Fig. 3(b and c)), indicating that the robust monoclinic structure with reversible V valence changes, which contributes to the excellent electrochemical performance of LVP/C electrode. This scenario is also verified by the V K-edge XAS results as shown in Fig. S1, which clearly demonstrates the reversible oxidation/reduction of V during the charge/discharge process [24,40,51]. It is worth mentioning that the spectral shape changes of vanadium are observed for both the surface (demonstrated by TEY spectra) and bulk (demonstrated by TFY spectra) of LVP/C electrodes, suggesting that the valence state of vanadium distributes homogeneously in the electrode materials when cycled in 3.0–4.3 V [52]. Such a homogeneous valence distribution inhibits the formation of Li-deficient phase that is related to the migration of the vanadium, which thus alleviates the capacity fading over cycling. Our results provide solid evidence that the faradaic reaction occurs both at the surface and in the bulk for LVP electrode during the discharge/charge process, resulting in the uniform valence state change of vanadium.

The highly reversible redox behavior of V during the charge/discharge process is further verified by O K-edge XAS results, as shown in Fig. 3(d and e). For the spectrum of pristine electrode, it can be divided into two distinct regions, with the features at 530–535 eV identified as  $t_{2g}$  and  $e_g$  bands originating from the O 2*p* and V 3*d* hybridization states and the broad features at

535–550 eV related to the O  $2p$  and V  $4sp/P\ 3sp$  hybridization states. During the charge process, a pre-edge feature located at  $\sim 529.5$  eV is gradually formed and its intensity reaches the maximum after charging to 4.3 V, which is attributed to the newly formed hybridization state between V  $3d$  states and O  $2p$  states as a consequence of V oxidation. The disappearance of this feature upon following discharge further confirms the reversible redox reaction of V in the first cycle. Interestingly, the highly reversible breathing behavior of the hybridization feature is also observed after 10 cycles, which is consistent with the V L-edge XAS results. Moreover, the O K-edge spectral evolution of the TEY data resembles that of the TFY data, which again implies the uniform electrochemical reaction throughout the surface and bulk of LVP. All these results suggest the reduced side reaction at the electrode-electrolyte interface (e.g. cathode surface phase transition, active material dissolution, passivation layer formation and electrolyte consumption), which should be responsible for the superior electrochemical performance of LVP/C electrode.

As a matter of fact, the hybridization strength of the O  $2p$  and V  $3d$  states can also affect the  $\text{PO}_4$  tetrahedral symmetry through the  $(\text{V-O-P-O})_n$  bonding arrangement in LVP, as proved by P K-edge XAS (Fig. S2) [40,53]. The feature at  $\sim 2150$  eV corresponds to the excitation of the P  $1s$  states to the unoccupied P  $3p$ -O  $2p$  hybridization states and its intensity gets suppressed during the charge process and enhanced during the discharge process, which is contrary to that of the O K-edge results. It is very likely that the enhanced O  $2p$ -V  $3d$  hybridization strength during the charge process shortens the V-O bond length, resulting the elongation of the P-O bonds accompanied by a lower formal P oxidation state and thereby a weaker O-P hybridization strength [54]. The oscillating behavior of this feature is also observed for the tenth cycle, which is in good agreement with the O K-edge and V L-edge XAS results.

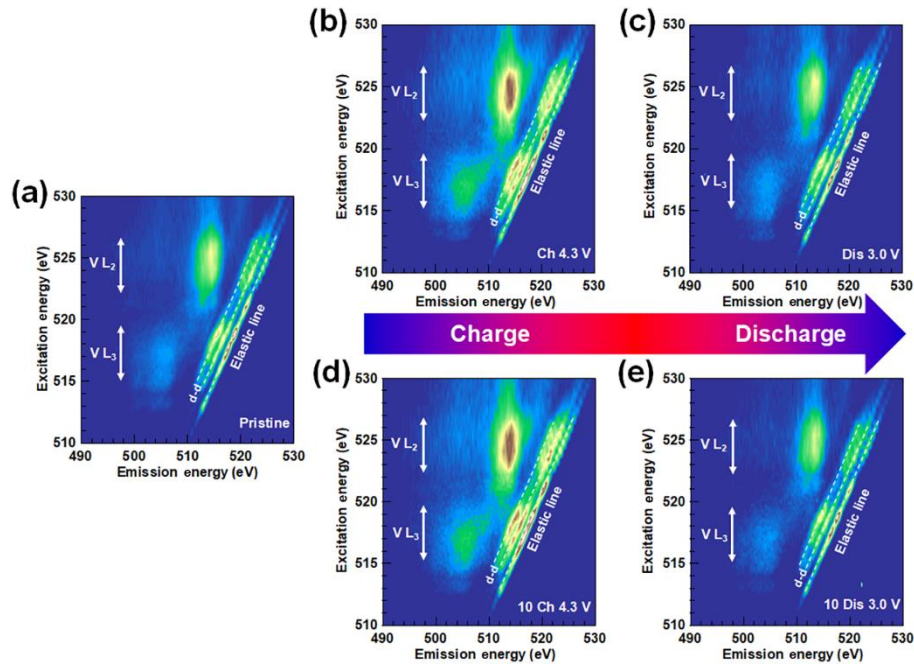


**Fig. 4.** Ex-situ V L-edge mRIXS characterization of LVP at different SOCs and cycle numbers. The measured samples are (a) pristine, (b) fully charged to 4.3 V, (c) fully discharged to 3.0 V, (d) fully charged to 4.3 V after 10 cycles, (e) fully discharged to 3.0 V. The bipolar arrows represent the fluorescence features (i.e.,  $V L_\alpha$  and  $V L_\beta$  bands) and the dashed lines mark the elastic line and  $d$ - $d$  excitations, respectively.

To further tackle the evolution of the occupied V  $3d$  states, we measured V L-edge mRIXS for LVP at fully charged and discharged states for the first and tenth cycles, as shown in Fig. 4. The advantage of mRIXS is that it provides energy distribution of the fluorescence signals during the XAS decay process [55–57]. The mRIXS of pristine electrode (Fig. 4a) mainly consists of three distinct features, including elastic line,  $d$ - $d$  excitations, and ordinary fluorescence features with fixed emission energies [58,59]. The fluorescence features include the  $V L_\alpha$  band (emission energy:  $\sim 508$  eV) and the  $V L_\beta$  band (emission energy:  $\sim 518$  eV), which is assigned to decay channels of  $V 3d \rightarrow V 2p_{3/2}$  and  $V 3d \rightarrow V 2p_{1/2}$ , respectively [59,60]. The V L-emission band is

dominated by the V 3d states strongly hybridized with O 2p states. The intensity of this state is greatly enhanced at charged state and depressed at discharged state for both the first and tenth cycles, indicating the highly reversible V redox reaction and thus the reversible V 3d-O 2p hybridization strength [25,49].

In addition to the V L-emission band, the evolution of *d-d* excitations also shows a strong dependence on the cycling conditions. For instance, the *d-d* excitation intensity is greatly enhanced from pristine (Fig. 4a) to fully charged states (Fig. 4(a and b)) and then depressed in the following discharge process (Fig. 4c). Similar behavior is also observed for the evolution of *d-d* excitation intensity during the tenth cycle. Because the *d-d* excitation intensity reflects the hybridization strength between the metal V 3d states and ligand O 2p states [61,62], the intensity change clearly indicates the increase/decrease of the hybridization strength during the charge/discharge process as a result of lithiation/delithiation, which is in good agreement with the corresponding XAS results.

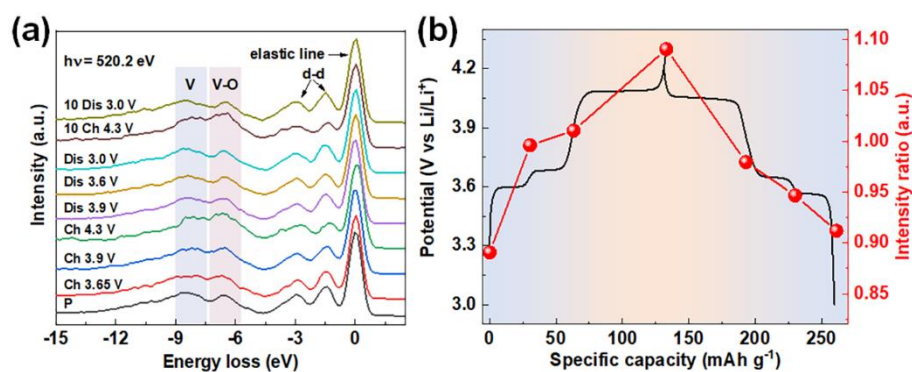


**Fig. 5.** (a) RIXS of LVP with an excitation energy of 520.2 eV. (b) Intensity ratio of the V 3d-O 2p hybridized states to the pure V 3d states as a function of SOC.

We further quantitatively analyzed the hybridization strength change of LVP using the RIXS spectra with an excitation energy of 520.2 eV (the position located between L<sub>3</sub> and L<sub>2</sub> in XAS) in

the energy loss manner (Fig. 5a). For the spectrum of pristine LVP, beside the elastic line and *d-d* excitation, two normal fluorescence emission features at  $\sim$ -8.5 and -6.5 eV are discerned, which corresponds to the pure V 3*d* states (denoted as V) and V 3*d* states hybridized with O 2*p* states (denoted as V-O), respectively [58,63]. The intensity evolutions of the pure V state and V-O state show opposite trend during the charge and discharge processes [20]. Similar behavior was also observed for the 10th cycle, as demonstrated in Fig. 5(a).

To further get a quantitative understanding of the hybridization strength change of LVP during cycling, we plotted the intensity ratio of these two states at different SOCs. As illustrated in Fig. 5(b), the intensity ratio remarkably increases during charge process and reaches to the maximum at 4.3 V where  $\text{Li}_3\text{V}_2(\text{PO}_4)_3$  loses two lithium and transforms to  $\text{LiV}_2(\text{PO}_4)_3$ , then gradually decreases in the subsequent discharge process as a consequence of the recovery of  $\text{Li}_3\text{V}_2(\text{PO}_4)_3$  [20,34]. After discharge back to 3.0 V, the intensity ratio nearly recovers to the pristine value, revealing the highly reversible phase transitions as in good accordance with the charge-discharge voltage profiles and CV curves. This quantitative analysis provides direct evidence of the high reversible redox reaction of V, which should be responsible for the remarkable electrochemical performance of LVP/C.

#### 4. Conclusions

We have performed a comprehensive investigation of the electrochemical performance and charge compensation mechanism of carbon decorated LVP for LIBs. The as-synthesized electrode material displays a remarkably high rate performance with a high capacity of 101 and 50 mAh  $\text{g}^{-1}$  even at 40 C and 100 C, respectively, together with an excellent long-term cycling life with a capacity retention of 87.1% after 1000 cycles at 20 C. Furthermore, the reaction mechanism was

studied using a combination of bulk- and surface-sensitive XAS and mRIXS. The spectroscopic results provide solid evidence that the faradaic reaction occurs both at the surface and in the bulk during the discharge/charge process with a high reversibility. This homogeneous valence distribution of V and O across the electrode material suggests the negligible side reaction at the electrode-electrolyte interface. In addition, the quantitative analysis of the intensity ratio between V  $3d$ -O  $2p$  hybridized states and pure V  $3d$  states further clearly verifies such a reversible redox reaction of vanadium, which should altogether account for the superior electrochemical performance of LVP/C. Our present study provides both effective synthesis strategy and valuable insights into the electrochemical reaction mechanism of LVP/C electrodes, which should boost the exploration of related electrode materials with high rate capability and long-term cycling performance.

### **Acknowledgments**

This work is supported by Collaborative Innovation Center of Suzhou Nano Science & Technology, the Priority Academic Program Development of Jiangsu Higher Education Institutions (PAPD), the 111 project, Joint International Research Laboratory of Carbon-Based Functional Materials and Devices, the National Natural Science Foundation of China (11905154), the Natural Science Foundation of the Jiangsu Higher Education Institutions of China (19KJA550004), the Natural Science Foundation of Jiangsu Province (BK20190814). Q. W. thanks to the National Key R&D Program of China (No. 2016YFA0202600), and the “Double-First Class” Foundation of Materials and Intelligent Manufacturing Discipline of Xiamen University. The work at Advanced Light Source of the Lawrence Berkeley National Laboratory is supported by the Director, Office of Science, Office of Basic Energy Sciences, of the U.S.

Department of Energy under Contract No. DE-AC02-05CH11231. The authors would like to thank SSRF (beamline 02B02) , ALS (beamline 8.0.1), and TLS (beamline 16A1) for the synchrotron beamtime.

## References

- [1] J.M. Tarascon, M. Armand, *Nature* 414(2001)359-367.
- [2] P.G. Bruce, S.A. Freunberger, L.J. Hardwick, J.M. Tarascon, *Nature Mater.* 11(1)(2012)19-29.
- [3] J.B. Goodenough, K.S. Park, *J. Am. Chem. Soc.* 135(4)(2013)1167-1176.
- [4] J.B. Goodenough, *J. Solid State Electrochem.* 16(6)(2012)2019-2029.
- [5] N.S. Choi, Z. Chen, S.A. Freunberger, X. Ji, Y.K. Sun, K. Amine, G. Yushin, L.F. Nazar, J. Cho, P.G. Bruce, *Angew. Chem. Int. Ed.* 51(40)(2012)9994-10024.
- [6] Z. Gong, Y. Yang, *Energy Environ. Sci.* 4(9)(2011)3223-3242.
- [7] M. Hu, X. Pang, Z. Zhou, *J. Power Sources* 237(2013)229-242.
- [8] V. Aravindan, J. Gnanaraj, Y.S. Lee, S. Madhavi, *J. Mater. Chem. A* 1(11)(2013)3518-3539.
- [9] L. Yuan, Z. Wang, W. Zhang, X. Hu, J. Chen, Y. Huang, J.B. Goodenough, *Energy Environ. Sci.* 4(2)(2011)269-284.
- [10] R. Sharabi, E. Markevich, V. Borgel, G. Salitra, G. Gershinshy, D. Aurbach, G. Semrau, M.A. Schmidt, N. Schall, C. Stinner, *J. Power Sources* 203(2012)109-114.
- [11] J. Wolfenstine, J. Allen, *J. Power Sources* 142(1-2)(2005)389-390.
- [12] Y. Luo, X. Xu, Y. Zhang, Y. Pi, Y. Zhao, X. Tian, Q. An, Q. Wei, L. Mai, *Adv. Energy Mater.* 4(16)(2014)1400107.
- [13] C. Liu, R. Massé, X. Nan, G. Cao, *Energy Storage Mater.* 4(2016)15-58.
- [14] A.R. Cho, J.N. Son, V. Aravindan, H. Kim, K.S. Kang, W.S. Yoon, W.S. Kim, Y.S. Lee, *J. Mater.*

Chem. 22(14)(2012)6556-6560.

[15] A. Pan, J. Liu, J. Zhang, W. Xu, G. Cao, Z. Nie, B.W. Arey, S. Liang, *Electrochem. Commun.* 12(12)(2010)1674-1677.

[16] S. Xun, J. Chong, X. Song, G. Liu, V.S. Battaglia, *J. Mater. Chem.* 22(31)(2012)15775-15781.

[17] J. Yan, W. Yuan, Z.Y. Tang, H. Xie, W.F. Mao, L. Ma, *J. Power Sources* 209(2012)251-256.

[18] Y. Cheng, H. Sang, Q. Jiang, H. Wang, H. Zhang, X. Li, *ACS Appl. Mater. Interfaces* 11(32)(2019)28934-28942.

[19] G. Zhou, L. Xu, G. Hu, L. Mai, Y. Cui, *Chem. Rev.* 119(20)(2019)11042-11109.

[20] Q. Wei, Q. An, D. Chen, L. Mai, S. Chen, Y. Zhao, K.M. Hercule, L. Xu, A. Minhas-Khan, Q. Zhang, *Nano Lett.* 14(2)(2014)1042-1048.

[21] P. Fu, Y. Zhao, Y. Dong, X. An, G. Shen, *J. Power Sources* 162(1)(2006)651-657.

[22] Y. Peng, R. Tan, J. Ma, Q. Li, T. Wang, X. Duan, *J. Mater. Chem. A* 7(24)(2019)14681-14688.

[23] Z. Gong, Y. Yang, *J. Energy Chem.* 27(6)(2018)1566-1583.

[24] S.M. Bak, R. Qiao, W. Yang, S. Lee, X. Yu, B. Anasori, H. Lee, Y. Gogotsi, X.Q. Yang, *Adv. Energy Mater.* 7(20)(2017)1700959.

[25] L. Zhang, D. Sun, Q. Wei, H. Ju, J. Feng, J. Zhu, L. Mai, E.J. Cairns, J. Guo, *J. Phys. D: Appl. Phys.* 51(49)(2018)494001.

[26] L. Zhang, Q. Wei, D. Sun, N. Li, H. Ju, J. Feng, J. Zhu, L. Mai, E.J. Cairns, J. Guo, *Nano Energy* 51(2018)391-399.

[27] C. Ma, J. Alvarado, J. Xu, R.J. Clement, M. Kodur, W. Tong, C.P. Grey, Y.S. Meng, *J Am Chem Soc* 139(13)(2017)4835-4845.

[28] J.L. Chen, C.C. Chang, Y.K. Ho, C.L. Chen, C.C. Hsu, W.L. Jang, D.H. Wei, C.L. Dong, C.W. Pao,

- J.F. Lee, J.M. Chen, J. Guo, M.K. Wu, *Phys. Chem. Chem. Phys.* 17(5)(2015)3482-3489.
- [29] J. Xu, M. Sun, R. Qiao, S.E. Renfrew, L. Ma, T. Wu, S. Hwang, D. Nordlund, D. Su, K. Amine, J. Lu, B.D. McCloskey, W. Yang, W. Tong, *Nat. Commun.* 9(1)(2018)947.
- [30] C. Cheng, S. Li, T. Liu, Y. Xia, L.Y. Chang, Y. Yan, M. Ding, Y. Hu, J. Wu, J. Guo, L. Zhang, *ACS applied materials & interfaces* 11(44)(2019)41304-41312.
- [31] Q. Li, R. Qiao, L.A. Wray, J. Chen, Z. Zhuo, Y. Chen, S. Yan, F. Pan, Z. Hussain, W. Yang, *J. Phys. D: Appl. Phys.* 49(41)(2016)413003.
- [32] X.J. Zhu, Y.X. Liu, L.M. Geng, L.B. Chen, *J. Power Sources* 184(2)(2008)578-582.
- [33] S.C. Yin, H. Grondey, P. Strobel, M. Anne, L.F. Nazar, *J. Am. Chem. Soc.* 125(34)(2003)10402-10411.
- [34] X. Rui, Q. Yan, M. Skyllas-Kazacos, T.M. Lim, *J. Power Sources* 258(2014)19-38.
- [35] X.H. Rui, N. Ding, J. Liu, C. Li, C.H. Chen, *Electrochim. Acta* 55(7)(2010)2384-2390.
- [36] Q. Chen, J. Wang, Z. Tang, W. He, H. Shao, J. Zhang, *Electrochim. Acta* 52(16)(2007)5251-5257.
- [37] G. Yang, H. Liu, H. Ji, Z. Chen, X. Jiang, *Electrochim. Acta* 55(8)(2010)2951-2957.
- [38] W.F. Mao, J. Yan, H. Xie, Z.Y. Tang, Q. Xu, *J. Power Sources* 237(2013)167-171.
- [39] J. Kang, V. Mathew, J. Gim, S. Kim, J. Song, W.B. Im, J. Han, J.Y. Lee, J. Kim, *Sci. Rep.* 4(2014)4047.
- [40] J. Yoon, S. Muhammad, D. Jang, N. Sivakumar, J. Kim, W.H. Jang, Y.S. Lee, Y.U. Park, K. Kang, W.S. Yoon, *J. Alloys Compd.* 569(2013)76-81.
- [41] S. Patoux, C. Wurm, M. Morcrette, G. Rousse, C. Masquelier, *J. Power Sources* 119-121(2003)278-284.
- [42] D. Liu, Z. Shadike, R. Lin, K. Qian, H. Li, K. Li, S. Wang, Q. Yu, M. Liu, S. Ganapathy, X. Qin,

- Q.H. Yang, M. Wagemaker, F. Kang, X.Q. Yang, B. Li, *Adv. Mater.* (2019)1806620.
- [43] Z. Shadike, E. Zhao, Y.-N. Zhou, X. Yu, Y. Yang, E. Hu, S. Bak, L. Gu, X.Q. Yang, *Adv. Energy Mater.* 8(17)(2018)1702588.
- [44] T. Schmitt, L.C. Duda, M. Matsubara, A. Augustsson, F. Trif, J.H. Guo, L. Gridneva, T. Uozumi, A. Kotani, J. Nordgren, *J. Alloys Compd.* 362(1-2)(2004)143-150.
- [45] X. Zhang, W. Yan, Y. Xie, *Chem. Asian J.* 6(12)(2011)3230-3235.
- [46] A. Gutierrez, R. Qiao, L. Wang, W. Yang, F. Wang, A. Manthiram, *Chem. Mater.* 26(9)(2014)3018-3026.
- [47] T. Schmitt, L.C. Duda, M. Matsubara, M. Mattesini, M. Klemm, A. Augustsson, J.H. Guo, T. Uozumi, S. Horn, R. Ahuja, A. Kotani, J. Nordgren, *Phys. Rev. B* 69(12)(2004)125103-125110.
- [48] D. Maganas, M. Roemelt, M. Havecker, A. Trunschke, A. Knop-Gericke, R. Schlogl, F. Neese, *Phys. Chem. Chem. Phys.* 15(19)(2013)7260-7276.
- [49] Y.R. Lu, T.Z. Wu, H.W. Chang, J.L. Chen, C.L. Chen, D.H. Wei, J.M. Chen, W.C. Chou, C.L. Dong, *Phys. Chem. Chem. Phys.* 19(22)(2017)14224-14229.
- [50] W. Duan, Z. Hu, K. Zhang, F. Cheng, Z. Tao, J. Chen, *Nanoscale* 5(14)(2013)6485-6490.
- [51] M. Pivko, I. Arcon, M. Bele, R. Dominko, M. Gaberscek, *J. Power Sources* 216(2012)145-151.
- [52] S. Chen, J. Zou, Y. Li, N. Li, M. Wu, J. Lin, J. Zhang, J. Cao, J. Feng, X. Niu, J. Bai, J. Qi, P. Gao, L. Wang, H. Li, *Nano Res.* 12(7)(2019)1675-1681.
- [53] H. Huang, S.C. Yin, T. Kerr, N. Taylor, L.F. Nazar, *Adv. Mater.* 14(2002)1525-1528.
- [54] S. Schmidt, S. Sallard, C. Borca, T. Huthwelker, P. Novak, C. Villevieille, *Chem. Commun.* 54(39)(2018)4939-4942.
- [55] L.J.P. Ament, M. van Veenendaal, T.P. Devereaux, J.P. Hill, J. van den Brink, *Rev. Mod. Phys.*

83(2)(2011)705-767.

[56] R. Thomas, J. Kas, P. Glatzel, M. Al Samarai, F.M.F. de Groot, R. Alonso Mori, M. Kavčič, M.

Zitnik, K. Bucar, J.J. Rehr, M. Tromp, *J. Phys. Chem. C* 119(2015)2419-2426.

[57] F. Marschall, Z. Yin, J. Rehanek, M. Beye, F. Doring, K. Kubicek, D. Raiser, S.T. Veedu, J. Buck,

A. Rothkirch, B. Rosner, V.A. Guzenko, J. Viehhaus, C. David, S. Techert, *Sci. Rep.* 7(1)(2017)8849.

[58] O.Y. Khyzhun, T. Strunskus, W. Grünert, C. Wöll, *J. Electron Spectrosc.* 149(1-3)(2005)45-50.

[59] T. Schmitt, L.C. Duda, A. Augustsson, J.H. Guo, J. Nordgren, J.E. Downes, C. Mcguinness, K.E.

Smith, G. Dhalenne, A. Revcolevschi, M. Klemm, S. Horn, *Surf. Rev. Lett.* 9(2002)1369-1374.

[60] T. Schmitt, A. Augustsson, L.C. Duda, J. Nordgren, J. Höwing, T. Gustafsson, *J. Appl. Phys.*

95(11)(2004)6444-6449.

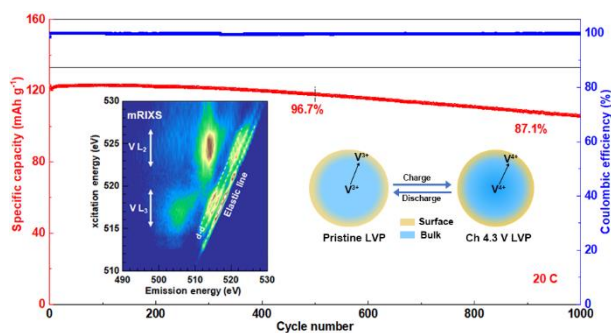
[61] H. Abe, M. Terauchi, M. Tanaka, S. Shin, Y. Ueda, *Jpn. J. Appl. Phys.* 36(1997)165-169.

[62] L. Braicovich, G. Ghiringhelli, L.H. Tjeng, V. Bisogni, C. Dallera, A. Piazzalunga, W. Reichelt,

N.B. Brookes, *Phys. Rev. B* 76(12)(2007)125105-125111.

[63] A. Meisel, K.H. Hallmeier, R. Szargan, *Phys. Scr.* 41(1990)513-516.

## TOC



The charge compensation mechanism of carbon decorated LVP for LIBs, which demonstrates a remarkably high rate performance together with an excellent long-term cycling life, has been comprehensively investigated by advanced X-ray spectroscopy techniques.